

Consequences of extended s_{\pm} -wave pairing in iron-based superconductors

Hsuan-Hao Fan¹, C. S. Liu², and W. C. Wu¹

¹*Department of Physics, National Taiwan Normal University, Taipei 11677, Taiwan*

²*Department of Physics, Yanshan University, Qinhuangdao 066004, China*

(Dated: August 13, 2018)

Motivated by a recent experiment of Song *et al.* [Science **332**, 1410 (2011)], we theoretically study the spin dynamics, charge dynamics, and point-contact Andreev-reflection spectroscopy (PCARS) of two-band iron-based superconductors of a possible extended s_{\pm} -wave pairing symmetry. We consider the case of a dominant s_{\pm} gap blended by a secondary extended s component in which gap nodes can develop in the Fermi pockets near zone corner and/or boundary. Due to the strong nesting effect associated with nodal regions, dynamical spin and charge susceptibilities can exhibit strong peaks at momenta near $(\pm\pi/2, 0)$, $(\pm\pi, \pm\pi/2)$, as well as $(\pm\pi, 0)$ in the unfolded Brillouin zone. For PCARS, considering an anisotropic band effect induced by an applied voltage, [100] differential conductance can exhibit a V -shape behavior manifesting a gap node occurring in such direction. It is highly suggested that the above features can be experimentally investigated to help sorting out the pairing symmetry of iron-based superconductors.

PACS numbers: 74.25.Ha, 74.20.Mn, 74.20.Rp, 74.50.+r

I. INTRODUCTION

Pairing symmetry of the Fe-based pnictide and chalcogenide superconductors is currently a hot topic in the study of superconductivity. While more and more experimental results have suggested that the order parameter in these materials is likely to be fully gapped s_{\pm} -wave,¹⁻⁴ whether there is a node in the gap remains controversially.^{5,6} For instance, in a recent scanning tunneling microscopy (STM) measurement of Song *et al.*,⁷ a nodal and two-fold symmetry gap is revealed in an iron selenide (FeSe) superconductor. It is no doubt that a central issue towards understanding the iron-based superconductors (FeSCs) is to unambiguously identify the pairing symmetry of these materials.

Among many different probes, inelastic neutron scattering (INS) measures the two-particle excitations and can give direct information on the momentum and energy dependence of the quasiparticle excitation and the pairing gap. A strong coherence peak can emerge in the dynamic spin susceptibility if the corresponding two-particle excitation is highly degenerate (i.e., in good nesting condition). In addition, strong peaks in INS can occur due to the resonant nature. A conclusive INS measurement of FeSCs remains unsettled however to which wave vectors of the strong peaks are observed to be remarkably material dependent. Some INS measurements have reported that spin resonances occur at the wave vector near (π, π) [or $(\pi, 0)$] in the folded (or unfolded) Brillouin zone (BZ) in 1111,⁸ 122,^{9,10} 111,¹¹ and 11 families.^{12,13} Other INS measurements on the new 122* family $A_x\text{Fe}_2\text{Se}_2$ ($A=\text{K, Rb, and Cs}$)¹⁴ of electron Fermi surfaces only^{15,16} have revealed that a resonance peak occurs at the wave vector $(\pi, \pi/2)$ in the unfolded BZ.¹⁷ On the theoretical side, on the other hand, prediction of the positions of the resonance peak in momentum space remains controversial. It has been predicted that for s_{\pm} pairing state, a strong coherence peak can exist in the

dynamic spin susceptibility $\chi(\mathbf{Q}, \omega)$ at the nesting wave vector $\mathbf{Q}=(0, \pi)$ or $(\pi, 0)$ in the unfolded BZ.¹⁸⁻²⁰ However, based on a pairing potential associated with the predicted $\chi(\mathbf{Q}, \omega)$, the SC state are found to be inconsistent with the previous prediction.^{21,22}

Charge dynamics which is accessible by high-energy electron scattering or X-ray scattering is another ideal candidate for studying the pairing symmetry of iron-based superconductors. While charge and spin susceptibilities are coupled to different coherence factors, as far as two-particle excitation is concerned they are qualitatively similar. Thus for a comparison point of view, it is also useful to theoretically study the charge dynamics within the same framework.

Another high-resolution phase-sensitive probe to detect the pairing symmetry is the point-contact Andreev-reflection spectroscopy (PCARS).²³⁻²⁵ The situations is still too early to make a conclusion however. Some PCARS measurements showed two coherent peaks and indicated that SC pairing state might be fully gapped on the Fermi surface (FS).²⁶⁻²⁸ Others showed a zero-bias conductance peak (ZBCP) and implied the presence of zero-energy bound states or Andreev bound state (ABS) on the interface.²⁹⁻³¹ Moreover, depending on the direction of the sample interface, some PCARSs have shown ZBCP coexisting with finite-energy coherent peaks.^{32,33} Most of theoretical studies so far have focused on the explanation of the ZBCP.^{34,35} It is important to carefully identify whether a gap node exists through the PCARS data.

In the current paper, we use a minimal two-orbital model³⁶ to study the spin dynamics, charge dynamics, and PCARS of FeSCs. Motivated by the recent STM experiment⁷ mentioned previously, we consider a pairing gap of a primary s_{\pm} -wave component plus a secondary extended s -wave component, called the extended s_{\pm} -wave state. In fact, this mixed pairing state is supported by a theoretical work of Yang *et al.*³⁷ who did a

variational quantum Monte Carlo calculation and concluded that both s_{\pm} -wave and extended s -wave pairings are equally energetically favorable in the five-band FeSCs. In the studies of spin and charge dynamics, it will be shown that in addition to wave vectors $(\pm\pi, 0)$ that most previous works focused on, strong coherence peaks can also occur around wave vectors $(\pm\pi/2, 0)$ and $(\pm\pi, \pm\pi/2)$, which is a unique feature in the extended s_{\pm} -wave state. In the studies of PCARS, considering an external anisotropy effect due to an applied bias voltage that leads to a relatively larger (smaller) Fermi pocket for β_1 - (β_2 -) band and hence a node can develop in the $(\pi, 0)$ direction in β_1 -band,³⁸ low-energy differential conductance dI/dV along the $[100]$ direction will feature a V -shape curve and manifests the existence of a node.

This paper is organized as follows. In Sec. II, we introduce the two-orbital model and especially show how the mixed gap behaves in different FSs as the secondary extended s -wave component changes. Sec. III is devoted to study the dynamical spin and charge susceptibilities for the model introduced in Sec. II. Section IV gives a theoretical study of the PCARS. Sec. V is a brief summary. For self sustainability, Appendix A gives detailed forms of the irreducible spin and charge response functions of a two-band superconductor. A brief discussion of Random-Phase Approximation (RPA) on the vertex-corrected spin and charge response functions is given in Appendix B.

II. MODEL

We consider a minimal two-orbital model for iron-based superconductors in which both d_{xz} and d_{yz} orbitals, coupled by the d_{xy} orbital, are considered in a two-dimensional square lattice. The Hamiltonian is³⁶

$$H_0 = \sum_{\mathbf{k}\sigma} \psi_{\mathbf{k}\sigma}^\dagger \begin{bmatrix} \epsilon_x(\mathbf{k}) - \mu & \epsilon_{xy}(\mathbf{k}) \\ \epsilon_{xy}(\mathbf{k}) & \epsilon_y(\mathbf{k}) - \mu \end{bmatrix} \psi_{\mathbf{k}\sigma}, \quad (1)$$

where $\psi_{\mathbf{k}\sigma}^\dagger \equiv [d_{x\sigma}^\dagger(\mathbf{k}), d_{y\sigma}^\dagger(\mathbf{k})]$ with $d_{x\sigma}^\dagger(\mathbf{k})$ [$d_{y\sigma}^\dagger(\mathbf{k})$] creating an electron in orbital d_{xz} (d_{yz}) of wave vector \mathbf{k} and spin σ and

$$\begin{aligned} \epsilon_x(\mathbf{k}) &= -2t_1 \cos k_x - 2t_2 \cos k_y - 4t_3 \cos k_x \cos k_y, \\ \epsilon_y(\mathbf{k}) &= -2t_2 \cos k_x - 2t_1 \cos k_y - 4t_3 \cos k_x \cos k_y, \\ \epsilon_{xy}(\mathbf{k}) &= -4t_4 \sin k_x \sin k_y. \end{aligned} \quad (2)$$

Here t_1, t_2 are the nearest-neighbor hoppings and t_3, t_4 are the next-nearest-neighbor hoppings. After Bogoliubov transformation, Hamiltonian (1) becomes

$$H_0 = \sum_{\mathbf{k}, \sigma, \nu=\pm} \xi_\nu(\mathbf{k}) \gamma_{\nu\sigma}^\dagger(\mathbf{k}) \gamma_{\nu\sigma}(\mathbf{k}), \quad (3)$$

where the band dispersions

$$\xi_{\pm}(\mathbf{k}) = \epsilon_{\pm}(\mathbf{k}) \pm \sqrt{\epsilon_{-}^2(\mathbf{k}) + \epsilon_{xy}^2(\mathbf{k})} - \mu \quad (4)$$

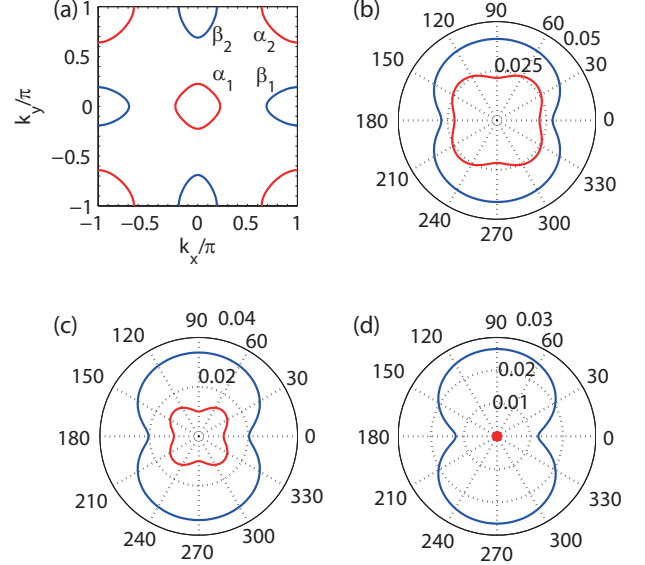


FIG. 1. (Color online) Frame (a): Fermi surfaces of the two-band model in the unfolded BZ. Red (blue) curves correspond to the hole (electron) Fermi pockets α_1 and α_2 (β_1 and β_2). Frame (b)-(d): Gap magnitudes around the α_2 (red) and β_1 (blue) FSs for mixing ratio (b) $x = 0$, (c) $x = 0.2$, and (d) $x = 0.4$ respectively.

with $\epsilon_{\pm}(\mathbf{k}) \equiv [\epsilon_x(\mathbf{k}) \pm \epsilon_y(\mathbf{k})]/2$ and $\gamma_{\nu\sigma}(\mathbf{k})$ is the band operator which destroys a quasiparticle of wave vector \mathbf{k} and spin σ in band ν . Operators $d_{r\sigma}(\mathbf{k})$ ($r = x, y$) and $\gamma_{\nu\sigma}(\mathbf{k})$ ($\nu = \pm$) are related to each other via the transformation

$$d_{r\sigma}(\mathbf{k}) = \sum_{\nu=\pm} a_{\nu}^r(\mathbf{k}) \gamma_{\nu\sigma}(\mathbf{k}), \quad (5)$$

where

$$\begin{aligned} a_{+}^x(\mathbf{k}) &= a_{-}^y(\mathbf{k}) = \text{sgn}[\epsilon_{xy}(\mathbf{k})] \left[\frac{1}{2} + \frac{\epsilon_{-}(\mathbf{k})}{2\sqrt{\epsilon_{-}^2(\mathbf{k}) + \epsilon_{xy}^2(\mathbf{k})}} \right]^{\frac{1}{2}} \\ a_{+}^y(\mathbf{k}) &= -a_{-}^x(\mathbf{k}) = \left[\frac{1}{2} - \frac{\epsilon_{-}(\mathbf{k})}{2\sqrt{\epsilon_{-}^2(\mathbf{k}) + \epsilon_{xy}^2(\mathbf{k})}} \right]^{\frac{1}{2}}. \end{aligned} \quad (6)$$

Considering a spin-singlet pairing state, the following BCS mean-field interaction Hamiltonian

$$H_{\text{SC}} = - \sum_{\mathbf{k}, \nu=\pm} [\Delta_{\nu}(\mathbf{k}) \gamma_{\nu\uparrow}^\dagger(\mathbf{k}) \gamma_{\nu\downarrow}^\dagger(-\mathbf{k}) + \text{H.c.}] \quad (7)$$

can be added to H_0 in (3). We consider the gap function being in the extended s_{\pm} state:

$$\begin{aligned} \Delta_{\nu}(\mathbf{k}) &= \Delta_1 \cos k_x \cos k_y + \frac{\Delta_2}{2} (\cos k_x + \cos k_y) \\ &\equiv \Delta_0 \left[(1-x) \cos k_x \cos k_y + \frac{x}{2} (\cos k_x + \cos k_y) \right] \end{aligned} \quad (8)$$

where a secondary extended s component ($\propto \Delta_2$) is added to the dominant s_{\pm} component ($\propto \Delta_1$).^{7,37} A “mixing ratio” x is introduced in the second line of (8) for convenience. For simplicity, the gap functions are taken to be the same in both bands.

Fig. 1(a) plots the FSs of the two-band model in which there are two hole Fermi pockets [α_1 and α_2 associated with $\xi_-(\mathbf{k}_F) = 0$] and two electron Fermi pockets [β_1 and β_2 associated with $\xi_+(\mathbf{k}_F) = 0$]. The parameters used are $t_1 = -0.8$, $t_2 = 1.4$, $t_3 = t_4 = -0.9$, and chemical potential $\mu = 1.15$.³⁸ All energies are in units of $t(> 0)$ which is material dependent. In Figs. 1(b)-1(d), we plot the gap magnitudes associated with α_2 - and β_1 -band FSs by varying the mixing ratio x and with a fixed amplitude $\Delta_0 = 0.05$ (also in units of t). The gaps associated with α_2 - and β_1 -band FSs are of particular interest in the current context, which will become clear shortly. As shown in Figs. 1(b)-1(d), gap magnitude on the α_2 FS decreases as the mixing ratio x increases. In particular, in the case of $x = 0.4$ [see Fig. 1(d)], the gap magnitude around α_2 band can reduce to zero (*i.e.*, becomes nodal). Note that the gap magnitude around the α_1 band (not shown) remains roughly unchanged as x changes. In addition, of equal importance, the gap magnitude around the β_1 -band FS becomes smaller and smaller in the k_x axis as x increases. When x is increased to be roughly 0.7, or when there is an induced band anisotropy due to an applied voltage with $x = 0.4$ (see Fig. 5), a gap node can actually develop in the β_1 Fermi pocket in the k_x direction.

III. SPIN AND CHARGE DYNAMICS

This section is devoted to study the dynamical spin and charge susceptibilities of FeSCs. To save the space here and still for self sustainability, detailed forms of the irreducible spin and charge response functions of a two-band superconductor are to be given in Appendix A. A brief discussion of the Random-Phase Approximation (RPA) on the vertex-corrected spin and charge response functions is given in Appendix B.

A. Dynamic Spin Susceptibility

We first consider the dynamical spin susceptibility in the $T \rightarrow 0$ limit. For spin-singlet pairing, dynamical spin susceptibility is proportional to the imaginary part of the spin response function defined as

$$\chi_{+-}(\mathbf{q}, i\omega_n) = \sum_{r,t} \int_0^\beta d\tau e^{i\omega_n \tau} \langle T_\tau S_r^+(\mathbf{q}, \tau) S_t^-(\mathbf{-q}, 0) \rangle, \quad (9)$$

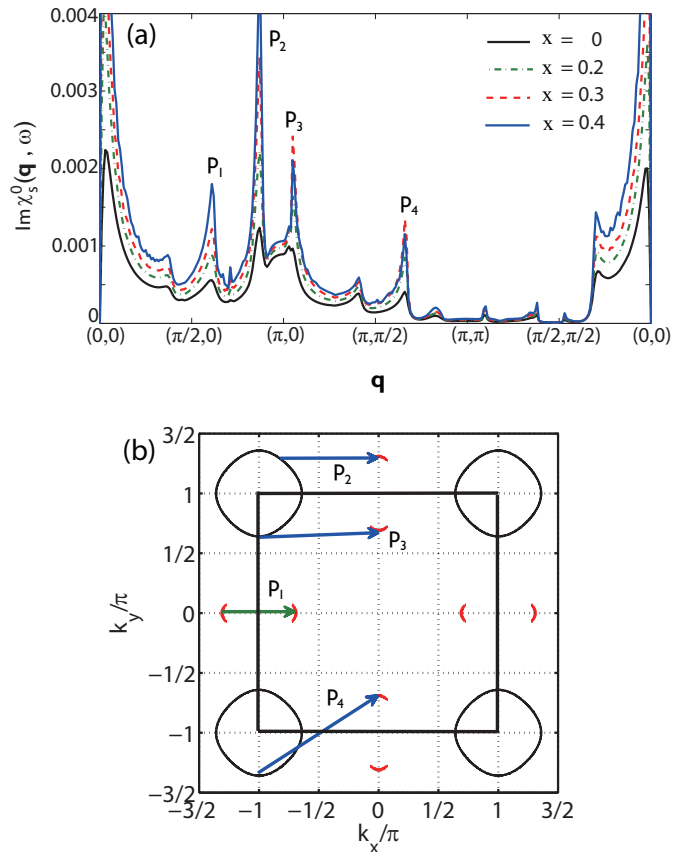


FIG. 2. (Color online) (a) Irreducible dynamic spin susceptibility $\text{Im}\chi_s^0(\mathbf{q}, \omega = 0.3\Delta_0)$ for wavevectors \mathbf{q} along the $(0,0) \rightarrow (\pi,0) \rightarrow (\pi,\pi) \rightarrow (0,0)$ route in the BZ and for different mixing ratio x . (b) Contour plot of the excitation spectrum $E_{\mathbf{k}} = \omega/2 = 0.15\Delta_0$ with $x = 0.4$. Blue arrows (p_2 - p_4) correspond to nesting wave vectors between the hole α_2 (black) and electron β_1 (red) bands. The one green arrow (p_1) corresponds to a nesting wave vector within the electron β_1 band. These vectors correspond to those peaks emerging in frame (a).

where $r, t = x, y$ are the orbital indices and the spin operator

$$S_r^+(\mathbf{q}, \tau) = \sum_{\mathbf{k}} d_{r\uparrow}^\dagger(\mathbf{k} + \mathbf{q}, \tau) d_{r\downarrow}(\mathbf{k}, \tau) = [S_r^-(\mathbf{-q}, \tau)]^\dagger. \quad (10)$$

For simplicity, we denote $\chi_s \equiv \chi_{+-}$ throughout this paper. In the $T \rightarrow 0$ limit, only the first and second terms contribute in the irreducible spin response function χ_s^0 given in Eq. (A1) in Appendix A. Furthermore, only the first term contributes if $\omega > 0$ is concerned. Consequently, apart from the effect of the coherence factors, the contributions to $\text{Im}\chi_s^0$ are dominated by the condition of the particle-particle excitation

$$\omega = E_{\nu'}(\mathbf{k} + \mathbf{q}) + E_\nu(\mathbf{k}). \quad (11)$$

Here $E_\nu(\mathbf{k}) = \sqrt{\xi_\nu^2(\mathbf{k}) + |\Delta_\nu(\mathbf{k})|^2}$ is the quasiparticle excitation spectrum with the band index $\nu = +, -$.

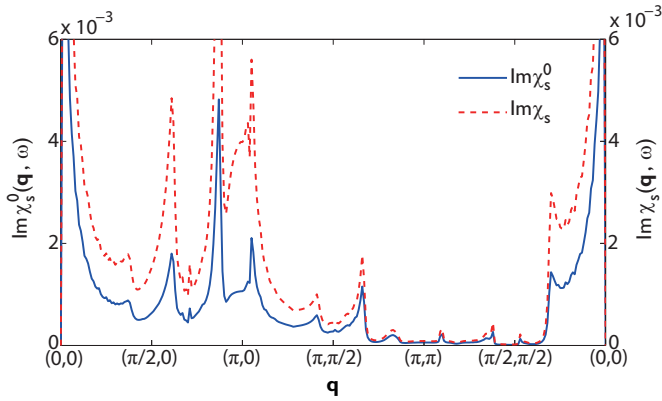


FIG. 3. (Color online) Comparison of the spectra in irreducible and RPA-corrected spin susceptibility $\text{Im}\chi_s^0$ and $\text{Im}\chi_s$ for $x = 0.4$ and $\omega = 0.3\Delta_0$. Coulomb repulsion is taken to be $U = 1.8$ for $\text{Im}\chi_s$.

In Fig. 2(a), we show the calculating results of the irreducible spin susceptibility $\text{Im}\chi_s^0$ for four different mixing ratio x and a fixed (low) energy $\omega = 0.3\Delta_0$. This two-dimensional plot is made by connecting important symmetry points in the BZ. As shown in Fig. 2(a), $\text{Im}\chi_s^0$ has strong peaks emerging at wave vectors near $(\pi/2, 0)$, $(\pi, 0)$, and $(\pi, \pi/2)$. Of most interest, with the same broadening $\delta = 0.01$ (in units of t) and the same gap amplitude Δ_0 used in all cases, the peaks are seen to be much stronger in the larger x cases compared to those in the pure s_{\pm} -wave ($x = 0$) case. To understand these phenomena, one just considers the low-energy particle-particle excitations with respect to the gap mixing. For pure s_{\pm} -wave pairing ($x = 0$) case, Fermi surfaces are fully gapped and consequently low-energy particle-particle excitation is suppressed. In contrast, for extended s_{\pm} -wave pairing of larger x , gap nodes can develop around the α_2 -band FSs as well as in certain \mathbf{k} areas around the β -band FSs. Consequently low-energy particle-particle excitation is enabled. (Note that no low-energy excitation with $\omega < \Delta_0$ is allowed in connection with the fully gapped α_1 -band FS regardless of what the mixing ratio x is.)

To understand the origins of the peaks further, in Fig. 2(b) we plot energy contours of the quasiparticle excitation $E_{\mathbf{k}} = \omega/2 = 0.15\Delta_0$ with $x = 0.4$. The arrows denote the nesting wave vectors for which degenerate strong two-particle excitations are associated with. These particular wave vectors, labeled by $p_1 \sim p_4$, are exactly those that the strong peaks are associated with in Fig. 2(a). As a matter of the fact, strong peaks emerge due to the scattering between electron and hole Fermi pockets (blue vectors) as well as within the same electron Fermi pocket (green vector).

To see how the behaviors of the full spin susceptibility differ from those of the irreducible one, in Fig. 3 we compare the results of $\text{Im}\chi_s^0$ and $\text{Im}\chi_s$ for $x = 0.4$ and $\omega = 0.3\Delta_0$. Here the full spin response function χ_s is calculated under RPA. A brief discussion on how χ_s is ob-

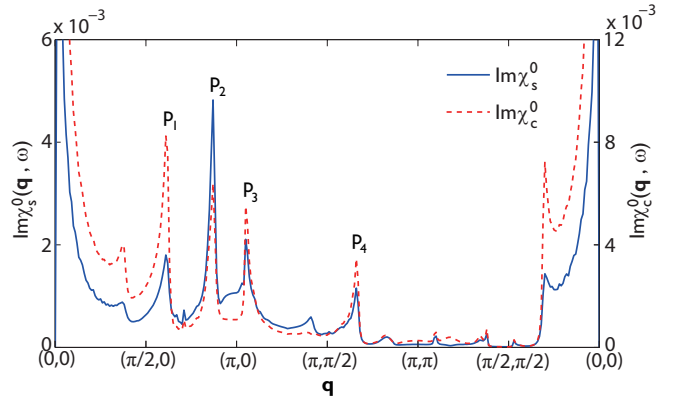


FIG. 4. (Color online) Comparison of the spectra in irreducible spin and charge susceptibilities $\text{Im}\chi_s^0$ and $\text{Im}\chi_c^0$ for $x = 0.4$ as $\omega = 0.3\Delta_0$.

tained is given in Appendix B. In calculating χ_s , we have set the intra-orbital Coulomb repulsion $U = 1.8$ (in units of t) and the Hund's coupling $J = 0$ (see Appendix B). In view of Fig. 3, while enhancement occurs for $\text{Im}\chi_s$, the results are qualitatively similar between $\text{Im}\chi_s^0$ and $\text{Im}\chi_s$. Concerning the results of $\text{Im}\chi_s^0$ and/or $\text{Im}\chi_s$ in Fig. 3, we note the following two facts. First, the spectra for a higher (lower) energy with $\omega > 0.3\Delta_0$ ($\omega < 0.3\Delta_0$) are basically the same as those of the $\omega = 0.3\Delta_0$ case. The only major difference is that the intensity of the peaks is stronger (weaker) in the higher (lower) energy case. Secondly, in the parameter regime we are studying, the peak around $\mathbf{q} = (\pi, 0)$ is enhanced most in $\text{Im}\chi_s$. Perhaps this is the case of most interest as most current INS experiments have focused on the possible magnetic peaks around $\mathbf{q} = (\pi, 0)$.^{8–13} We emphasize that strong magnetic peaks can also emerge at wave vectors around $(\pi/2, 0)$ and $(\pi, \pi/2)$ if an extended s_{\pm} -wave pairing state of a larger mixing ratio x is present.

B. Dynamic Charge Susceptibility

We now turn to study the dynamical charge susceptibility in the $T \rightarrow 0$ limit. Dynamical charge susceptibility is proportional to the imaginary part of the charge response function

$$\chi_c(\mathbf{q}, i\omega_n) = \sum_{r,t} \int_0^\beta d\tau e^{i\omega_n \tau} \langle T_\tau \rho_r(\mathbf{q}, \tau) \rho_t(-\mathbf{q}, 0) \rangle, \quad (12)$$

where the density operator

$$\rho_r(\mathbf{q}, \tau) = \sum_{\mathbf{k}\sigma} d_{r\sigma}^\dagger(\mathbf{k} + \mathbf{q}, \tau) d_{r\sigma}(\mathbf{k}, \tau). \quad (13)$$

The detailed form of the irreducible charge response function, χ_c^0 , is given in Eq. (A2) in Appendix A. In Fig. 4, we show and compare the spectra of the irreducible charge and spin susceptibilities $\text{Im}\chi_c^0$ and $\text{Im}\chi_s^0$ for $x = 0.4$ and $\omega = 0.3\Delta_0$. One sees clearly that similar strong peaks

emerge at wave vectors near $(\pi/2, 0)$, $(\pi, \pi/2)$ as well as $(\pi, 0)$ in both $\text{Im}\chi_s^0$ and $\text{Im}\chi_c^0$. Therefore the charge peaks with wave vectors near $(\pi/2, 0)$, $(\pi, \pi/2)$, and $(\pi, 0)$ can also be considered as the signature for the extended s_{\pm} -wave pairing state. One is noted a key difference in the spectra of $\text{Im}\chi_s^0$ and $\text{Im}\chi_c^0$ however. In $\text{Im}\chi_s^0$, the strongest peak is associated with wavevector p_2 , while in $\text{Im}\chi_c^0$, the strongest peak is associated with wavevector p_1 . The difference is due to different coherence factors coupled to χ_c^0 and χ_s^0 [see the first term of χ_s^0 and χ_c^0 in Eqs. (A1) and (A2)].

IV. POINT-CONTACT ANDREEV-REFLECTION SPECTROSCOPY

When a free electron is injected from a normal metal into a superconductor (forming an interface at $x = 0$) with an incident angle θ , there are two possible reflections. One is the normal reflection (reflected as electrons) and another is the Andreev reflection (reflected as holes, due to electron and hole coupling in the \mathbf{k} subspace). The resulting wave function Ψ_N in the normal side ($x < 0$) can be obtained by the superposition of the above two kinds of reflected waves and the incident wave. In the superconducting side ($x > 0$), the resulting wave function Ψ_S is the superposition of the electron-like and hole-like quasiparticle wave functions, which can be obtained by solving the Andreev equation.

One key issue for the superconductor is that electron-like and hole-like quasiparticles will experience the effective pairing potential $\Delta(\theta)$ and $\Delta(\pi - \theta)$ respectively. As a matter of fact, resulting tunneling conductance will depend strongly on the pairing symmetry and the direction of the tunneling current. Considering tunneling current along the [100] direction, $\Delta(\theta) = \Delta(\pi - \theta)$ for the current extended s_{\pm} -wave pairing and tunneling conductance will feature a nodeless gap if the mixing ratio x is small. However, as mentioned before, when x is large or when there is a large band anisotropy occurring due to an applied voltage (see later), the gap associated with the β_1 -band will shrink in the k_x direction and could eventually develop a node in such direction. This nodal gap will then be manifested in the tunneling conductance along such direction.

By matching the normal and superconducting wave functions and their derivatives at the interface $x = 0$:

$$\begin{aligned} \psi_N(\mathbf{r})|_{x=0^-} &= \psi_S(\mathbf{r})|_{x=0^+}, \\ \frac{2mH}{\hbar^2}\psi_S(\mathbf{r})|_{x=0^+} &= \frac{d\psi_S(\mathbf{r})}{dx}|_{x=0^+} - \frac{d\psi_N(\mathbf{r})}{dx}|_{x=0^-}, \end{aligned} \quad (14)$$

where H denotes the strength of a delta-function like barrier potential $V(x) \equiv H\delta(x)$, one can solve the normal and Andreev reflection coefficients r_N and r_A . With the solved r_N and r_A and based on the well-known formula for the conductance $\sigma_S = 1 + |r_A|^2 - |r_N|^2$ (see, for example, Ref. [39]), the normalized differential conductance

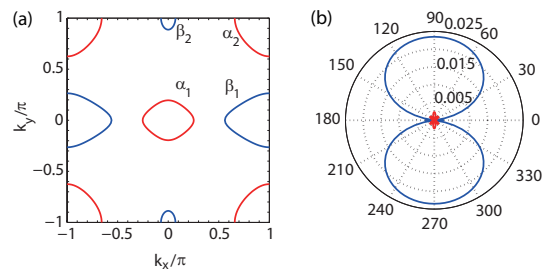


FIG. 5. (Color online) (a) Fermi surfaces of the band dispersions given in (17). The parameters are the same as those in Fig. 1(a) together with an anisotropy $\delta\epsilon = 0.3$. (b) Gap magnitudes of the extended s_{\pm} -wave gap (8) associated with α_2 - (red) and β_1 -band (blue) FSs with $x = 0.4$ and $\Delta_0 = 0.05$.

dI/dV can be obtained to be

$$\tilde{\sigma}_S(E, \theta) = \frac{16(1 + \Gamma^2)\cos^4\theta + 4Z^2(1 - \Gamma^2)\cos^2\theta}{|4\cos^2\theta + Z^2(1 - \Gamma^2)|^2}, \quad (15)$$

where $Z = 2mH/\hbar^2$ is the effective potential barrier and

$$\Gamma \equiv \frac{E}{|\Delta(\theta)|} - \sqrt{\left(\frac{E}{|\Delta(\theta)|}\right)^2 - 1}. \quad (16)$$

In a real experimental setup, the above derivation is equivalent to consider an STM tip made of a normal metal and being well point-contacted to the superconductor. Similar derivations of Eqs. (15) and (16) can be found in Ref. [24] where a single-band system was considered.

In the current context, for simplicity, we assume that the two bands are decoupled completely. Nevertheless the resulting tunneling conductance is considered to be contributed by all α_1 , α_2 , β_1 , and β_2 FSs. To see the possible nodal effect for the conductance current along the [100] direction, we consider a band anisotropy effect induced by an applied voltage. The applied voltage should be much larger than the pairing gap magnitude.³⁸ Consequently the induced anisotropic band dispersion can be approximated by

$$\tilde{\xi}_{\pm}(\mathbf{k}) = \epsilon_{\pm}(\mathbf{k}) \pm \sqrt{(\epsilon_{-}(\mathbf{k}) + \delta\epsilon)^2 + \epsilon_{xy}^2(\mathbf{k})} - \mu, \quad (17)$$

where $\delta\epsilon$ denotes the induced anisotropy. In Fig. 5(a), FSs of the anisotropic band (17) are shown in which β_1 -band Fermi pocket becomes larger, while β_2 -band Fermi pocket becomes smaller as compared to those in Fig. 1(a). The parameters used in Fig. 5(a) are the same as those in Fig. 1(a), *i.e.*, $t_1 = -0.8$, $t_2 = 1.4$, $t_3 = t_4 = -0.9$, and $\mu = 1.15$. In addition, the induced anisotropy is chosen to be $\delta\epsilon = 0.3$. Fig. 5(b) shows how the extended s_{\pm} -wave gap behaves in the α_2 - and β_1 -band FSs with $x = 0.4$ and $\Delta_0 = 0.05$. The most important feature in these gaps is that gap nodes develop in both α_2 - and β_1 -band FSs. For the α_2 -band gap, the node appears to be nodal almost everywhere around the α_2 FS. In contrast, for the

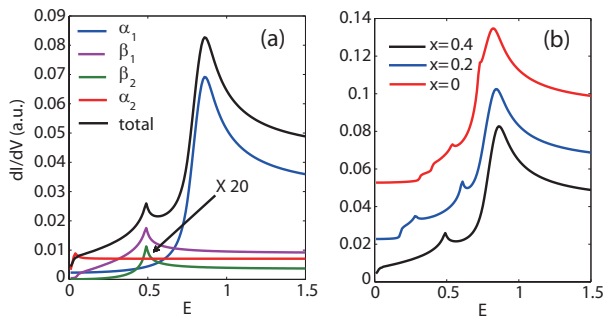


FIG. 6. (Color online) (a) Resulting [100] differential conductance dI/dV vs. tunneling voltage E (black line). Parameters are the same as those in Fig. 5. For comparison, contributions due to four Fermi pockets are plotted respectively in which β_2 contribution is magnified by a factor of 20 for a better view. (b) Comparison of resulting [100] $dI/dV(E)$ curves with $x = 0.4, 0.2$, and 0 . For clarity the curve of $x = 0.2$ (0) is shifted by 0.02 (0.04) vertically.

β_1 -band gap, the node appears in the k_x direction only which should have a strong effect on the conductance current along the [100] direction.

Figure 6(a) plots the [100] differential conductance dI/dV versus the tunneling voltage E for a normal-superconducting junction. The superconductor is made of the two-band iron-based with the induced anisotropic band dispersions given in (17) and the extended s_{\pm} -wave pairing gap given in (8). The parameters used are the same as those in Fig. 5. In addition, the strength of barrier is taken to be $H = 10$ (in units of t). To be more explicitly, $dI/dV(E)$ is obtained by integrating $\tilde{\sigma}_S(E, \theta)$ in (15) over the θ angle from $-\pi/2$ to $\pi/2$. For comparison purpose, we have plotted the contribution respectively due to $\alpha_1, \alpha_2, \beta_1$, and β_2 bands. Of most interest is that, in the low E regime, in contrast to α_1, α_2 , and β_2 bands whose contribution is either little or almost independent of E , the contribution due to β_1 band is dominant and linear in E . This can be understood in the following. β_2 -band is located far away from the k_x axis, thus its contribution (green line) to the differential conductance is the least. For the α_2 -band, the gap is nodal almost everywhere on the FS, so its contribution to $dI/dV(E)$ (red line) is almost independent of E (*i.e.*, obeying the Ohm's law). For the α_1 -band, finite s -wave gap is fully developed in its FS, consequently its corresponding $dI/dV(E)$ (blue line) exhibits a U shape. In contrast for the β_1 -band, gap node develops in the k_x direction, so for the [100] differential conductance, it exhibits a V shape (purple line) and manifests the existence of a gap node along such direction. The overall V -shape $dI/dV(E)$ at low E seems to be in consistency with the STM measurement reported in Ref. [7].

In Fig. 6(b), we show the [100] dI/dV versus E by changing the gap mixing ratio x . It is evident that when

$x = 0$ for a pure s_{\pm} -wave pairing, all FSs are fully gapped and consequently the resulting $dI/dV(E)$ exhibits a U -shape behavior. Those tiny peaks corresponds to quasi-particle excitations associated with different Fermi surfaces. It is in great contrast to the case of $x = 0.4$ in which $dI/dV(E)$ exhibits a V -shape behavior, as already shown in Fig. 6(a).

V. SUMMARY

In this paper, motivated by the recent experiment of Song *et al.*⁷, we intend to study the spin dynamics, charge dynamics, and point-contact Andreev-reflection spectroscopy (PCARS) of iron-based superconductors of a possible extended s_{\pm} -wave pairing symmetry. We consider a minimal two-band model in which superconducting gap is dominated by the s_{\pm} component but mixed by a secondary extended s component. Comparing to the pure s_{\pm} -wave gap of finite gaps around all four Fermi pockets, in the present extended s_{\pm} -wave pairing state, gap nodes can develop in the Fermi pockets near the zone corner and/or the zone boundary. Useful signatures associated with the possible nodes are identified in spin dynamics, charge dynamics, as well as in the PCARS. It is hoped that the features discussed in this paper can be carefully investigated by experiments to help sorting out the pairing symmetry of iron-based superconductors.

Finally we remark that some recent inelastic neutron scattering experiments on $K_x\text{Fe}_2\text{Se}_2$ samples have uncovered magnetic resonance peak at $\mathbf{q} = (\pi, \pi/2)$ in unfolded BZ.¹⁷ This implies that the pairing state in these materials is likely to be d -wave. Fermi surface topology in these materials is, in fact, quite different from the iron-based superconductors that we are considering.

ACKNOWLEDGMENTS

This work was supported by National Science Council of Taiwan (Grant No. NSC 99-2112-M-003-006-MY3). CSL was supported by Hebei Provincial Natural Science Foundation of China (Grant No. A2010001116) and the National Natural Science Foundation of China (Grant No. 10974169). We also acknowledge the support from the National Center for Theoretical Sciences, Taiwan.

Appendix A: Irreducible Spin and Charge Response Functions

Within the two-orbital model proposed by Raghu *et al.*,³⁶ irreducible spin and charge response functions can be derived to be (see also the derivation in Ref. [40])

$$\begin{aligned} \chi_s^0(\mathbf{q}, \omega) = & -\frac{1}{2N} \sum_{\mathbf{k}} \sum_{r,t} \sum_{\nu, \nu'=\pm} M_{rt}^{\nu\nu'}(\mathbf{k}, \mathbf{q}) \left[A_{\mathbf{k}, \mathbf{q}}^- \frac{1 - f(E_{\nu'}(\mathbf{k})) - f(E_{\nu}(\mathbf{k} + \mathbf{q}))}{\omega - E_{\nu'}(\mathbf{k}) - E_{\nu}(\mathbf{k} + \mathbf{q}) + i\delta} - B_{\mathbf{k}, \mathbf{q}}^- \frac{1 - f(E_{\nu'}(\mathbf{k})) - f(E_{\nu}(\mathbf{k} + \mathbf{q}))}{\omega + E_{\nu'}(\mathbf{k}) + E_{\nu}(\mathbf{k} + \mathbf{q}) + i\delta} \right. \\ & \left. - C_{\mathbf{k}, \mathbf{q}}^+ \frac{f(E_{\nu'}(\mathbf{k})) - f(E_{\nu}(\mathbf{k} + \mathbf{q}))}{\omega - E_{\nu'}(\mathbf{k}) + E_{\nu}(\mathbf{k} + \mathbf{q}) + i\delta} + D_{\mathbf{k}, \mathbf{q}}^+ \frac{f(E_{\nu'}(\mathbf{k})) - f(E_{\nu}(\mathbf{k} + \mathbf{q}))}{\omega + E_{\nu'}(\mathbf{k}) - E_{\nu}(\mathbf{k} + \mathbf{q}) + i\delta} \right] \equiv \sum_{rt} \chi_{s,rt}^0(\mathbf{q}, \omega) \end{aligned} \quad (\text{A1})$$

$$\begin{aligned} \chi_c^0(\mathbf{q}, \omega) = & -\frac{1}{N} \sum_{\mathbf{k}} \sum_{r,t} \sum_{\nu, \nu'=\pm} M_{rt}^{\nu\nu'}(\mathbf{k}, \mathbf{q}) \left[A_{\mathbf{k}, \mathbf{q}}^+ \frac{1 - f(E_{\nu'}(\mathbf{k})) - f(E_{\nu}(\mathbf{k} + \mathbf{q}))}{\omega - E_{\nu'}(\mathbf{k}) - E_{\nu}(\mathbf{k} + \mathbf{q}) + i\delta} - B_{\mathbf{k}, \mathbf{q}}^+ \frac{1 - f(E_{\nu'}(\mathbf{k})) - f(E_{\nu}(\mathbf{k} + \mathbf{q}))}{\omega + E_{\nu'}(\mathbf{k}) + E_{\nu}(\mathbf{k} + \mathbf{q}) + i\delta} \right. \\ & \left. - C_{\mathbf{k}, \mathbf{q}}^- \frac{f(E_{\nu'}(\mathbf{k})) - f(E_{\nu}(\mathbf{k} + \mathbf{q}))}{\omega - E_{\nu'}(\mathbf{k}) + E_{\nu}(\mathbf{k} + \mathbf{q}) + i\delta} + D_{\mathbf{k}, \mathbf{q}}^- \frac{f(E_{\nu'}(\mathbf{k})) - f(E_{\nu}(\mathbf{k} + \mathbf{q}))}{\omega + E_{\nu'}(\mathbf{k}) - E_{\nu}(\mathbf{k} + \mathbf{q}) + i\delta} \right] \equiv \sum_{rt} \chi_{c,rt}^0(\mathbf{q}, \omega), \end{aligned} \quad (\text{A2})$$

where $r, t = x, y$ correspond to the orbital indices, $\nu, \nu' = \pm$ correspond to the band indices, N is the renormalization factor, and δ is the broadening. $f(E_{\nu}(\mathbf{k}))$ is the Fermi distribution function with $E_{\nu}(\mathbf{k}) = \sqrt{\xi_{\nu}^2(\mathbf{k}) + |\Delta(\mathbf{k})|^2}$ the quasiparticle excitation spectrum, $\xi_{\nu}(\mathbf{k})$ the band dispersion, and $\Delta_{\nu}(\mathbf{k})$ the superconducting gap. The coherence factors in (A1) and (A2) are respectively

$$\begin{aligned} A_{\mathbf{k}, \mathbf{q}}^{\pm} & \equiv \frac{1}{2} \left[\left(1 + \frac{\xi_{\nu'}(\mathbf{k})}{E_{\nu'}(\mathbf{k})} \right) \left(1 - \frac{\xi_{\nu}(\mathbf{k} + \mathbf{q})}{E_{\nu}(\mathbf{k} + \mathbf{q})} \right) \right. \\ & \quad \left. \pm \frac{\Delta_{\nu'}(\mathbf{k}) \Delta_{\nu}(\mathbf{k} + \mathbf{q})}{E_{\nu'}(\mathbf{k}) E_{\nu}(\mathbf{k} + \mathbf{q})} \right] \\ B_{\mathbf{k}, \mathbf{q}}^{\pm} & \equiv \frac{1}{2} \left[\left(1 - \frac{\xi_{\nu'}(\mathbf{k})}{E_{\nu'}(\mathbf{k})} \right) \left(1 + \frac{\xi_{\nu}(\mathbf{k} + \mathbf{q})}{E_{\nu}(\mathbf{k} + \mathbf{q})} \right) \right. \\ & \quad \left. \pm \frac{\Delta_{\nu'}(\mathbf{k}) \Delta_{\nu}(\mathbf{k} + \mathbf{q})}{E_{\nu'}(\mathbf{k}) E_{\nu}(\mathbf{k} + \mathbf{q})} \right] \\ C_{\mathbf{k}, \mathbf{q}}^{\pm} & \equiv \frac{1}{2} \left[\left(1 + \frac{\xi_{\nu'}(\mathbf{k})}{E_{\nu'}(\mathbf{k})} \right) \left(1 + \frac{\xi_{\nu}(\mathbf{k} + \mathbf{q})}{E_{\nu}(\mathbf{k} + \mathbf{q})} \right) \right. \\ & \quad \left. \pm \frac{\Delta_{\nu'}(\mathbf{k}) \Delta_{\nu}(\mathbf{k} + \mathbf{q})}{E_{\nu'}(\mathbf{k}) E_{\nu}(\mathbf{k} + \mathbf{q})} \right] \\ D_{\mathbf{k}, \mathbf{q}}^{\pm} & \equiv \frac{1}{2} \left[\left(1 - \frac{\xi_{\nu'}(\mathbf{k})}{E_{\nu'}(\mathbf{k})} \right) \left(1 - \frac{\xi_{\nu}(\mathbf{k} + \mathbf{q})}{E_{\nu}(\mathbf{k} + \mathbf{q})} \right) \right. \\ & \quad \left. \pm \frac{\Delta_{\nu'}(\mathbf{k}) \Delta_{\nu}(\mathbf{k} + \mathbf{q})}{E_{\nu'}(\mathbf{k}) E_{\nu}(\mathbf{k} + \mathbf{q})} \right] \end{aligned} \quad (\text{A3})$$

and the function

$$M_{rt}^{\nu\nu'}(\mathbf{k}, \mathbf{q}) \equiv a_{\nu}^r(\mathbf{k} + \mathbf{q}) a_{\nu'}^t(\mathbf{k}) a_{\nu'}^t(\mathbf{k}) a_{\nu}^t(\mathbf{k} + \mathbf{q}), \quad (\text{A4})$$

with $a_{\nu}^r(\mathbf{k})$ defined in Eq. (6).

Appendix B: Random-Phase Approximation

Here we consider the full spin and charge response functions taking into account the vertex correction due to

various interactions. For d_{xz} - and d_{yz} -orbital electrons, we consider the following on-site interaction

$$\begin{aligned} H_I = & U \sum_{ir} n_{i,r\uparrow} n_{i,r\downarrow} + \frac{V}{2} \sum_{i,r,t \neq r} n_{ir} n_{it} \\ & - \frac{J}{2} \sum_{i,r,t \neq r} \mathbf{S}_{ir} \cdot \mathbf{S}_{it} \\ & + \frac{J'}{2} \sum_{i,r,t \neq r} \sum_{\sigma} d_{ir\sigma}^{\dagger} d_{ir\bar{\sigma}}^{\dagger} d_{it\bar{\sigma}} d_{it\sigma}, \end{aligned} \quad (\text{B1})$$

where U and V correspond to the intra- and inter-orbital Coulomb repulsion respectively, J is the Hund's coupling, and J' is responsible for pair hopping. Note in (B1), for each site i , $n_{ir} = n_{i,r\uparrow} + n_{i,r\downarrow}$. Within Random-Phase Approximation, irreducible spin response function in (A1) will be renormalized to be

$$\hat{\chi}_s(\mathbf{q}, \omega) = \hat{\chi}_s^0(\mathbf{q}, \omega) [\mathbf{I} - \Gamma_s \hat{\chi}_s^0(\mathbf{q}, \omega)]^{-1}, \quad (\text{B2})$$

where \mathbf{I} is the 2×2 unit matrix, $\hat{\chi}_s^0$ is a 2×2 matrix formed by the intra- and inter-orbital spin susceptibilities defined in the last term in (A1), *i.e.*, $[\hat{\chi}_s^0]_{rt} \equiv \chi_{s,rt}^0$, and the vertex matrix

$$\Gamma_s = \begin{pmatrix} U & J/2 \\ J/2 & U \end{pmatrix}. \quad (\text{B3})$$

While the irreducible charge response function in (A2) will be renormalized to be

$$\hat{\chi}_c(\mathbf{q}, \omega) = \hat{\chi}_c^0(\mathbf{q}, \omega) [\mathbf{I} + \Gamma_c \hat{\chi}_c^0(\mathbf{q}, \omega)]^{-1}, \quad (\text{B4})$$

where $[\hat{\chi}_c^0]_{rt} \equiv \chi_{c,rt}^0$ and

$$\Gamma_c = \begin{pmatrix} U & 2V \\ 2V & U \end{pmatrix}. \quad (\text{B5})$$

In the calculation of $\text{Im}\chi_s$ in Sec. III, we have chosen $U = 1.8$ and $J = 0$ for simplicity. We do not actually calculate the RPA-corrected $\text{Im}\chi_c$ in the current context.

- ¹ K. Umezawa, Y. Li, H. Miao, K. Nakayama, Z.-H. Liu, P. Richard, T. Sato, J. B. He, D.-M. Wang, G. F. Chen, H. Ding, T. Takahashi, and S.-C. Wang, *Phys. Rev. Lett.* **108**, 037002 (2012).
- ² C.-T. Chen, C. C. Tsuei, M. B. Ketchen, Z.-A. Ren, and Z. X. Zhao, *Nat. Phys.* **6**, 260 (2010).
- ³ T. Hanaguri, S. Niitaka, K. Kuroki, and H. Takagi, *Science* **328**, 474 (2010).
- ⁴ K. Hashimoto, T. Shibauchi, T. Kato, K. Ikada, R. Okazaki, H. Shishido, M. Ishikado, H. Kito, A. Iyo, H. Eisaki, S. Shamoto, and Y. Matsuda, *Phys. Rev. Lett.* **102**, 017002 (2009).
- ⁵ C. W. Hicks, T. M. Lippman, M. E. Huber, J. G. Analytis, J.-H. Chu, A. S. Erickson, I. R. Fisher, and K. A. Moler, *Phys. Rev. Lett.* **103**, 127003 (2009).
- ⁶ J. K. Dong, S. Y. Zhou, T. Y. Guan, H. Zhang, Y. F. Dai, X. Qiu, X. F. Wang, Y. He, X. H. Chen, and S. Y. Li, *Phys. Rev. Lett.* **104**, 087005 (2010).
- ⁷ C.-L. Song, Y.-L. Wang, P. Cheng, Y.-P. Jiang, W. Li, T. Zhang, Z. Li, K. He, L. Wang, J.-F. Jia, H.-H. Hung, C. Wu, X. Ma, X. Chen, and Q.-K. Xue, *Science* **332**, 1410 (2011).
- ⁸ S.-i. Shamoto, M. Ishikado, A. D. Christianson, M. D. Lumsden, S. Wakimoto, K. Kodama, A. Iyo, and M. Arai, *Phys. Rev. B* **82**, 172508 (2010).
- ⁹ A. D. Christianson, E. A. Goremychkin, R. Osborn, S. Rosenkranz, M. D. Lumsden, C. D. Malliakas, I. S. Todorov, H. Claus, D. Y. Chung, M. G. Kanatzidis, R. I. Bewley, and T. Guidi, *Nature* **456**, 930 (2008).
- ¹⁰ M. Ishikado, Y. Nagai, K. Kodama, R. Kajimoto, M. Nakamura, Y. Inamura, S. Wakimoto, H. Nakamura, M. Machida, K. Suzuki, H. Usui, K. Kuroki, A. Iyo, H. Eisaki, M. Arai, and S.-i. Shamoto, *Phys. Rev. B* **84**, 144517 (2011).
- ¹¹ A. E. Taylor, M. J. Pitcher, R. A. Ewings, T. G. Perring, S. J. Clarke, and A. T. Boothroyd, *Phys. Rev. B* **83**, 220514 (2011).
- ¹² Y. Qiu, W. Bao, Y. Zhao, C. Broholm, V. Stanev, Z. Tesanovic, Y. C. Gasparovic, S. Chang, J. Hu, B. Qian, M. Fang, and Z. Mao, *Phys. Rev. Lett.* **103**, 067008 (2009).
- ¹³ H. A. Mook, M. D. Lumsden, A. D. Christianson, S. E. Nagler, B. C. Sales, R. Jin, M. A. McGuire, A. S. Sefat, D. Mandrus, T. Egami, and C. dela Cruz, *Phys. Rev. Lett.* **104**, 187002 (2010).
- ¹⁴ R. H. Liu, X. G. Luo, M. Zhang, A. F. Wang, J. J. Ying, X. F. Wang, Y. J. Yan, Z. J. Xiang, P. Cheng, G. J. Ye, Z. Y. Li, and X. H. Chen, *Europhys. Lett.* **94**, 27008 (2011).
- ¹⁵ T. Qian, X.-P. Wang, W.-C. Jin, P. Zhang, P. Richard, G. Xu, X. Dai, Z. Fang, J.-G. Guo, X.-L. Chen, and H. Ding, *Phys. Rev. Lett.* **106**, 187001 (2011).
- ¹⁶ Y. Zhang, L. X. Yang, M. Xu, Z. R. Ye, F. Chen, C. He, H. C. Xu, J. Jiang, B. P. Xie, J. J. Ying, X. F. Wang, X. H. Chen, J. P. Hu, M. Matsunami, S. Kimura, and D. L. Feng, *Nat. Mater.* **10**, 273 (2011).
- ¹⁷ G. Friemel, J. T. Park, T. A. Maier, V. Tsurkan, Y. Li, J. Deisenhofer, H.-A. Krug von Nidda, A. Loidl, A. Ivanov, B. Keimer, and D. S. Inosov, *Phys. Rev. B* **85**, 140511 (2012).
- ¹⁸ I. I. Mazin, D. J. Singh, M. D. Johannes, and M. H. Du, *Phys. Rev. Lett.* **101**, 057003 (2008).
- ¹⁹ M. M. Korshunov and I. Eremin, *Phys. Rev. B* **78**, 140509 (2008).
- ²⁰ T. A. Maier and D. J. Scalapino, *Phys. Rev. B* **78**, 020514 (2008).
- ²¹ T. Das and A. V. Balatsky, *Phys. Rev. B* **84**, 014521 (2011).
- ²² T. A. Maier, S. Graser, P. J. Hirschfeld, and D. J. Scalapino, *Phys. Rev. B* **83**, 100515 (2011).
- ²³ C.-R. Hu, *Phys. Rev. Lett.* **72**, 1526 (1994).
- ²⁴ Y. Tanaka and S. Kashiwaya, *Phys. Rev. Lett.* **74**, 3451 (1995).
- ²⁵ G. Deutscher, *Rev. Mod. Phys.* **77**, 109 (2005).
- ²⁶ P. Szabó, Z. Pribulová, G. Pristáš, S. L. Bud'ko, P. C. Canfield, and P. Samuely, *Phys. Rev. B* **79**, 012503 (2009).
- ²⁷ M. Tortello, D. Daghero, G. A. Umharino, V. A. Stepanov, J. Jiang, J. D. Weiss, E. E. Hellstrom, and R. S. Gonnelli, *Phys. Rev. Lett.* **105**, 237002 (2010).
- ²⁸ D. Tortello, M. Daghero, G. Umharino, R. Gonnelli, V. Stepanov, and J. Kim, *J. Supercond. Nov. Magn.* **22**, 553 (2009).
- ²⁹ L. Shan, Y. Wang, X. Zhu, G. Mu, L. Fang, C. Ren, and H.-H. Wen, *Europhys. Lett.* **83**, 57004 (2008).
- ³⁰ K. A. Yates, L. F. Cohen, Z.-A. Ren, J. Yang, W. Lu, X.-L. Dong, and Z.-X. Zhao, *Supercond. Sci. Technol.* **21**, 092003 (2008).
- ³¹ X. Lu, W. K. Park, H. Q. Yuan, G. F. Chen, G. L. Luo, N. L. Wang, A. S. Sefat, M. A. McGuire, R. Jin, B. C. Sales, D. Mandrus, J. Gillett, S. E. Sebastian, and L. H. Greene, *Supercond. Sci. Technol.* **23**, 054009 (2010).
- ³² Y.-L. Wang, L. Shan, L. Fang, P. Cheng, C. Ren, and H.-H. Wen, *Supercond. Sci. Technol.* **22**, 015018 (2009).
- ³³ K. A. Yates, K. Morrison, J. A. Rodgers, G. B. S. Penny, J.-W. G. Bos, J. P. Attfield, and L. F. Cohen, *New J. Phys.* **11**, 025015 (2009).
- ³⁴ M. A. N. Araújo and P. D. Sacramento, *Phys. Rev. B* **79**, 174529 (2009).
- ³⁵ S. Onari and Y. Tanaka, *Phys. Rev. B* **79**, 174526 (2009).
- ³⁶ S. Raghu, X.-L. Qi, C.-X. Liu, D. J. Scalapino, and S.-C. Zhang, *Phys. Rev. B* **77**, 220503 (2008).
- ³⁷ F. Yang, H. Zhai, F. Wang, and D.-H. Lee, *Phys. Rev. B* **83**, 134502 (2011).
- ³⁸ H.-H. Hung, C.-L. Song, X. Chen, X. Ma, Q.-k. Xue, and C. Wu, *Phys. Rev. B* **85**, 104510 (2012).
- ³⁹ G. E. Blonder, M. Tinkham, and T. M. Klapwijk, *Phys. Rev. B* **25**, 4515 (1982).
- ⁴⁰ K. Masuda and S. Kurihara, *J. Phys. Soc. Jpn.* **79**, 074710 (2010).